Nature Communications

https://doi.org/10.1038/s41467-026-70643-5

Article in Press

Structural basis and regulation of GSDME pore formation

Received: 13 February 2026

Accepted: 26 February 2026

Cite this article as: Teran, E., Tian, T., Wang, C. *et al.* Structural basis and regulation of GSDME pore formation. *Nat Commun* (2026). https://doi.org/10.1038/s41467-026-70643-5

Evelyn Teran, Tian Tian, Chengliang Wang, Xinzheng Wang, Jinghan Wang, Dongchun Ni, Vijay A. Rathinam & Jianbin Ruan

Structural basis and regulation of GSDME pore formation

Evelyn Teran[1,*], Tian Tian[1,*], Chengliang Wang[1], Xinzheng Wang[1], Jinghan Wang[2], Dongchun Ni[2,3], Vijay A Rathinam[1], and Jianbin Ruan[1,#]

1. Department of Immunology, University of Connecticut School of Medicine, Farmington, CT, USA;
2. Department of medicine, Shenzhen University Medical School, Shenzhen, China;
3. Laboratory of Biological Electron Microscopy (LBEM), Institute of Physics (IPHYS), School of Basic Sciences (SB), EPFL;

* These authors contribute equally.

\# Correspondence: ruan@uchc.edu

Abstract

Gasdermins (GSDMs) are pore-forming proteins that mediate pyroptosis and contribute to inflammatory and cancer-related processes. Although GSDME shares structural similarity with other gasdermins, its activation and pore assembly mechanisms remain incompletely defined. Here we determine high-resolution cryo-electron microscopy structures of 27- and 28-fold human GSDME pores at 3.64 Å and 3.58 Å resolution. The structures reveal conserved structural architecture together with distinct features, including an extended transmembrane β-barrel and a comparatively compact membrane-engagement geometry. Structure-guided mutagenesis identifies lipid-binding and oligomerization interfaces required for pore formation. We further demonstrate that caspase-3 activates GSDME through direct recognition of a DMPD tetrapeptide motif within the interdomain linker, independently of the GSDME C-terminal domain. Following proteolytic activation, *S*-palmitoylation of GSDME N-terminal domain enhances pore-forming efficiency, with Cys180 serving as the primary functional site. Together, these findings establish a coordinated structural and regulatory framework in which proteolytic licensing and lipid modification sequentially control GSDME pore formation.

Introduction

Gasdermins are a family of pore-forming proteins that execute pyroptosis, a lytic and proinflammatory form of programmed cell death critical for host defense and inflammatory responses[1-4]. Upon proteolytic activation by inflammatory caspases or other enzymes[5-15], gasdermins release their pore-forming active N-terminal (NT) domains, which undergo conformational changes and oligomerize on the plasma membrane to form large transmembrane β-barrel pores, ultimately compromising membrane integrity and inducing cell lysis[16-19]. Among the gasdermin family members, GSDMA to GSDME and DFNB59, GSDMD and GSDME are the most extensively studied due to their pivotal roles in innate immunity and cancer.

While GSDMD is cleaved by inflammatory caspases such as caspase-1, -4, -5, and -11 during canonical and non-canonical inflammasome activation[5,6], GSDME is specifically cleaved by granzyme B and apoptotic caspase-3, linking apoptosis and pyroptosis[7,8,15]. In the context of chemotherapy or immune effector-mediated killing, caspase-3 activation leads to GSDME cleavage and pyroptotic, rather than apoptotic, death of tumor cells, enhancing anti-tumor immunity[8]. Thus, GSDME is emerging as a critical effector at the intersection of cell death pathways with therapeutic implications.

Despite the recognized biological roles of GSDME, the structural mechanisms of GSDME pore formation and regulation have remained poorly understood. Previous structural studies have characterized the pores formed by GSDMA3, GSDMB, and GSDMD, revealing conserved features such as a membrane-inserting β-barrel and a crown-like globular subdomain[18-21]. However, whether GSDME shares these architectural features, and how its distinct sequence properties influence its pore assembly and membrane engagement, and functions, have remained unknown. Furthermore, the regulatory mechanisms beyond pore-formation, such as proteolytic

cleavage and posttranslational modifications like palmitoylation and PARylation[22-26], remain incompletely characterized for GSDME.

In this study, we use single-particle cryo-electron microscopy (cryo-EM) to determine high-resolution structures of human GSDME pores and define the molecular basis of its membrane binding and oligomerization. Our structure-function analysis reveals both conserved and distinct conformational features in GSDME pore, including the longest transmembrane β-barrel among gasdermins and a compact membrane engagement conformation. In addition, we show that unlike GSDMD, GSDME is recognized and cleaved by caspase-3 through recognition of the specific tetrapeptide motif (DMPD) within the interdomain linker, independently of the GSDME C-terminal (CT) domain. Finally, we identify a palmitoylated cysteine residue within the GSDME-NT that enhances GSDME pyroptotic activity. Together, our findings provide critical structural and mechanistic insights into GSDME pore formation and regulation, establishing a molecular framework for future studies on its role in diseases.

Results

Cryo-EM structure of GSDME pore

Pore structures of GSDME were determined using single particle cryo-EM. GSDME pores were reconstituted on cardiolipin-containing liposomes and subsequently solubilized using the detergent octaethylene glycol monododecyl ether (C12E8). Detergent-solubilized GSDME pores were further purified through size-exclusion chromatography (SEC). SEC fractions containing GSDME pores were then subjected to both negative-stain EM and cryo-EM analysis (Supplementary Fig.S1a-d). Both EM analysis revealed extensive, well-behaved GSDME pore assemblies solubilized from liposomes (Supplementary Fig.S1e, f). In addition to fully closed ring-shaped pores, arc-shaped and slit-like GSDME oligomers were also observed (Supplementary

Fig.S1e), consistent with previous reports which showed that such incomplete assemblies are also capable of membrane permeabilization[18-21,27-31]. Although two-dimensional (2D) classification did not yield class averages with clear symmetry, likely due to the tilted particle orientations, 3D classification without imposed symmetry revealed GSDME pores comprising 27- and 28-fold symmetric assemblies as the predominant populations (Supplementary Fig.S2a). Non-uniform refinement of these subsets with appropriate symmetry resulted in 3D reconstructions of the 27- and 28-fold-symmetric GSDME pores at resolutions of 3.64 Å and 3.58 Å, respectively (Supplementary Fig.S2; Table S1). The 28-fold pore exhibits an inner diameter of approximately 180 Å, an outer diameter of 280 Å, and a height of 80 Å (Fig.1a). This pore size closely resembles that of the 27-fold GSDMA3 pore, but is slightly larger than the 24-26 fold GSDMB pores and smaller than the 31-34 fold GSDMD pores[18-21]. Like other gasdermin pores, the GSDME pore features a crown-like ring formed by the globular domains and a transmembrane β-barrel. Notably, the GSDME pore conduit is predominantly negatively charged (Fig.1b), similar to that in GSDMD. This acidic conduit would allow the passage of the basic mature cytokines[32], thus turning the tumor immune microenvironment from a “cold” into a “hot” state. In the pore, each GSDME-NT protomer adopts a hand-shaped architecture, in which the globular domain forms the “palm”, the α1 helix is the “thumb”, the β1-β2 loop is the “wrist”, and two extended β-hairpins constitute the “fingers” that insert into the membrane (Fig.1c).

Despite a conserved overall architecture, the GSDME pore also exhibits structural features that distinguish it from other gasdermin pores. Notably, GSDME forms the longest transmembrane β-barrel reported to date within the gasdermin family, with each β-strand comprising approximately 14 residues—compared to 12 in GSDMD and 11 in GSDMB and GSDMA3 (Supplementary Fig.S3a). As a result, the GSDME pore spans a lipid bilayer of approximately 40 Å in thickness, slightly exceeding the 30–35 Å traversed by GSDMD, GSDMB, and GSDMA3 pores[18-21] (Fig.1d). In addition, GSDME-NT adopts the a comparatively compact

conformation among characterized gasdermin pores, positioning its globular domain more proximal to the membrane surface. This compactness is reflected in the orientation angle between the “palm” (globular domain) and the “fingers” (membrane-inserting β-hairpins), which measures 77° in GSDME, narrower than those in GSDMD (121°), GSDMA3 (92°), and GSDMB (83°)[18-21] (Fig.1e), placing GSDME toward a comparatively compact conformation relative to other characterized gasdermin pores.

Membrane attachment of GSDME pore

Structural analysis shows that membrane attachment of the GSDME pore is primarily mediated by two key interfaces: the N-terminal α1 helix and the β1-β2 loop (Fig.2a). In lipid binding site 1 (BS1), basic residues K4, R7, and R11 within the helix α1 interact with the acidic head groups of membrane phospholipids (Fig.2a). While in BS2, hydrophobic residues F43, W44, and W46 in the β1-β2 loop form a hydrophobic tip that inserts into the lipid bilayer, serving as a membrane anchor. This anchor region is further stabilized by a flanking cluster of basic residues—K39, K40, K41, R42, R48, and K50, which interact with the acidic membrane surface (Fig.2a). In addition to BS1 and BS2, a less-conserved lipid binding site (BS3) is also observed in GSDME, contributed by K204 on the β8 strand (Fig.2a). To validate these structural observations, we generated GSDME mutants targeting BS1 (K4E/R7E/R11/E) and BS2 (K41E/R42E/R48E/K50E). Both sets of mutations completely abolished membrane-permeabilization ability in cardiolipin-containing liposomes and, critically, yielded the same phenotype in phosphatidylserine (PS)-containing, plasma membrane-mimicking liposomes (Fig.2b, Supplementary Fig.S3b). Furthermore, mutation of hydrophobic tip into glycines (F43G/W44G/W46G) moderately impaired the pore-forming activity of GSDME in both lipid contexts, while substitution with hydrophilic glutamic acid residues (F43E/W44E/W46E) resulted in a complete loss of activity across both cardiolipin and PS liposomes (Fig.2c, Supplementary Fig.S3b). In agreement, these mutations also markedly or entirely compromised the ability of the GSDME-NT to induce pyroptotic cell death (Fig.2d,

Supplementary Fig.S3c). It has to be mentioned that our earlier study identified an additional lipid binding site (BS4) in GSDMB formed by the C-terminus of the pore-forming domain[20]. BS4 provides extra contributions to protein-membrane interactions and plays an important role in modulating the pyroptotic activity of GSDMB, which is regulated by alternative splicing[20,21,33,34]. Although not highly conserved, a similar BS4 appears to be also present in GSDME, involving K240, and with potential contribution from R151 located in helix α3 (Fig.2e). Consistently, K240E and R151E/K240E mutants exhibit strongly reduced leakage in both cardiolipin- and PS-containing liposomes and diminished pyroptosis in cells (Fig.2d, f, and Supplementary Fig.S3b, c), confirming the functional importance of BS4 in GSDME pore formation.

GSDME pore oligomerization

The oligomerization interfaces in GSDME pore are structurally conserved relative to those of other gasdermin family members and are formed by contributions from both the globular domain and the transmembrane β-barrel region (Fig.2g). Within the globular domain, two major interfaces are observed: Interface I, mediated by interactions between the α3 helix of one subunit and the α2 helix together with the C-terminal linker region of an adjacent subunit, and Interface II, formed by end-on juxtaposition of the α1 helices from neighboring subunits (Fig.2h). Notably, several previously reported cancer-associated loss-of-function mutations, such as D14Y, D18V, N24D, R28I, and E245K, are located at or near these oligomerization interfaces[15] (Fig.2h), suggesting that these mutations may impair the pyroptotic activity of GSDME by disrupting pore assembly. Supporting this notion, we found that mutations of key residues in Interface I (R238G) or Interface II (N24G/N26G) markedly attenuated the ability of GSDME to induce liposome leakage in vitro in both cardiolipin- and PS-containing liposomes (Fig.2i, Supplementary Fig.S3b) and to trigger pyroptotic cell death in HEK293T cells (Fig.2d, and Supplementary Fig.S3c). While the overall architecture of pore assembly is conserved across GSDMs, the specific amino acid residues consisting of the oligomerization interfaces differ among family members (Supplementary

Fig.S3a). This sequence-level divergence within a conserved structural framework likely contributes to gasdermin-specific assembly properties and helps prevent cross-oligomerization between different gasdermins, while also complicating the prediction of pyroptotic potential based solely on conserved lipid-binding features.

Sequence-dependent cleavage of GSDME by caspase-3

Proteolytic cleavage of the full-length protein is a crucial step in the activation of GSDMs. Previous studies have proposed a dual-site engagement model for the caspase-1/-11 mediated activation of GSDMD, wherein the inflammatory caspases recognize the cleavage signature within the interdomain linker of GSDMD, and also interact with an enzyme-recruitment “exosite” located in GSDMD-CTD[35,36]. To determine whether caspase-3-mediated cleavage of GSDME follows a similar mechanism, we herein examined the interaction between caspase-3 and GSDME. Unexpectedly, size-exclusion chromatography showed that the caspase-3 catalytic domain (p17/p12 C163A) does not stably associate with GSDME (Fig.3a), in contrast to the previously observed complex formation between GSDMD and caspase-1/-11. Consistent with this, isothermal titration calorimetry (ITC) demonstrated a very weak interaction between full-length GSDME and caspase-3 (p17/p12), with a dissociation constant in the millimolar range and no detected interaction between GSDME-CTD and caspase-3 (p17/p12) (Fig.3b), suggesting that GSDME recognition by caspase-3 may occur through a distinct mechanism that might not involve the C-terminal domain.

To elucidate this mechanism, we generated a series of GSDME mutants (Fig.3c) and assessed their cleavage by active caspase-3 or caspase-11. As expected, wild-type (WT) GSDME and GSDMD were cleaved efficiently by active caspase-3 (Fig.3c). In contrast, substitution of the canonical caspase-3 cleavage site at residues 267–270 (DMPD) with either AAAD or FLTD completely abolished cleavage (Fig.3d), indicating that the tetrapeptide sequence

at the interdomain linker is essential for caspase-3 recognition. Notably, replacing the GSDME-CTD with that of GSDMD (Chimera^{DMPD}) did not impair caspase-3-mediated cleavage, whereas mutation of the $_{267}$DMPD$_{270}$ motif in this chimera protein (Chimera^{FLTD}) abolished the cleavage (Fig.3d). When these proteins were tested for caspase-11 cleavage, we observed that neither the wild-type GSDME nor the AAAD or FLTD mutants were cleaved (Fig.3e). However, both chimeric proteins containing the GSDMD-CTD were cleaved by caspase-11, regardless of the cleavage motif (Fig.3e), consistent with previous study that the GSDMD-CTD rather than the cleavage motif facilitates recognition by caspase-11. Interestingly, cleavage by caspase-11 also generated multiple truncated N-terminal fragments of chimeric GSDME (Fig.3e), likely due to the presence of aspartic acid residues in the flexible regions near the interdomain linker that serve as additional cleavage sites (Fig.3f).

Furthermore, to exclude a potential contribution of GSDME-NT to caspase-3 recognition, we introduced the GSDME interdomain linker containing the DMPD motif into human GSDMA, a gasdermin not reported to be cleaved by caspase-3. While WT GSDMA was refractory to caspase-3, the GSDMA^{DMPD} chimera was readily cleaved (Fig.3g), indicating that the DMPD tetrapeptide is sufficient to confer caspase-3 cleavage. Together, these results support a mechanism in which caspase-3 cleaves GSDME primarily through recognition of a specific tetrapeptide motif within the interdomain linker, independent of the C-terminal domain, in contrast to the dual-site engagement model proposed for GSDMD.

GSDME is palmitoylated at N-terminal domain

While caspase-3-mediated cleavage is necessary to release the pore-forming N-terminal domain of GSDME, proteolysis alone does not fully define the efficiency or extent of pore formation. Accumulating evidence has indicated that posttranslational modifications also play critical roles in modulating the pyroptotic activity of gasdermins. For example, *S*-palmitoylation of a conserved

residue Cys191 in GSDMD promotes pyroptosis by weakening autoinhibition and enhancing membrane localization[22-24,26]. GSDME is likewise subject to *S*-palmitoylation, particularly within its C-terminal domain[37]. Blocking palmitoylation through mutation or treating with palmitoylation inhibitor 2-bromopalmitate (2BP) reinforces the intramolecular interaction between its N- and C-terminal domains, thereby suppressing its pyroptotic function[37]. Notably, GSDME is also palmitoylated at its N-terminal domain[22]. However, whether this palmitoylation participates in regulating its pore-forming activity remains unclear, especially when the corresponding Cys191 is not conserved in GSDME (Supplementary Fig.S3a).

To orthogonally characterize the *S*-palmitoylation in GSDME-NT, we metabolically labeled HEK293T cells with palmitic acid alkyne and performed copper-catalyzed azide–alkyne cycloaddition ("click chemistry") to fluorescent tetramethylrhodamine (TAMRA)-azide for direct detection. Similar to that observed in GSDMD[22], GSDME-NT displayed a robust TAMRA signal and migrated as high-molecular-weight species consistent with oligomers under non-reducing SDS–PAGE (Fig.4a). Addition of reducing agent β-mercaptoethanol (β-ME) to treat the sample not only diminished the TAMRA signal through removal of thioester-linked *S*-palmitoylation form GSDME-NT but also collapsed the oligomeric bands, indicating that palmitoylation promotes oligomerization (Fig.4a). Therefore, GSDME-NT undergoes palmitoylation, which may regulate GSDME pore formation by facilitating oligomerization.

C180 is the primary palmitoylation site in GSDME

There are five cysteine residues in the N-terminal domain of GSDME, among which four localize in the globular domain and one in the transmembrane region (Fig.4b). To investigate whether these cysteines are palmitoylated and the role of palmitoylation in GSDME-NT, we employed an *S*-palmitoylation detection assay that converts the *S*-palmitoyl/acyl group on cysteine residues into a multifunctional-tag (MfTag) with a molecular weight of approximately 5

kDa. This approach enables the detection of palmitoylation through gel mobility shifts and, importantly, provides information on the number of palmitoylation sites present on the target protein (Fig.4c). As expected, GSDME-NT expressed in HEK293T cells was palmitoylated; however, unexpectedly, the pattern indicated multiple palmitoylation sites (Fig.4d). To further identify the specific palmitoylated residue(s), we analyzed a panel of GSDME-NT constructs in which individual cysteines were mutated to alanine. We found that mutations at C156, C168, or C235 did not alter the palmitoylation profile, whereas C45A and C180A each eliminated the higher-molecular-weight “x2” MfTag band observed in WT, consistent with two palmitoylation events in WT and identifying C45 and C180 as palmitoylated residues (Fig.4d). Importantly, the same palmitoylation pattern and site dependence were observed in additional cell types, including HeLa and 5637 human bladder carcinoma cells (Supplementary Fig.S4a), confirming the palmitoylation of C45 and C180 in GSDME-NT.

To determine whether these sites contribute to GSDME-mediated pore formation, we assessed the pyroptotic cell death induced by GSDME-NT and its mutants. Consistent with the palmitoylation data, mutations at the non-palmitoylated residues C168 and C235 had no effect on GSDME-NT induced pyroptosis. Interestingly, although C156 was not a palmitoylation site, its mutation moderately reduced cell death (Fig.4e, f, and Supplementary Fig.S4b). This effect is likely due to a structural perturbation upon mutation, as C156 is buried deeply within the globular domain of GSDME (Fig.4b). In contrast, C180A markedly impaired pyroptotic activity (Fig.4e, f, and Supplementary Fig.S4b). Similar to C191 in GSDMD, C180 is located within the transmembrane region of GSDME (Fig.4b), suggesting a conserved positional logic for palmitoylation-enhanced membrane engagement. Surprisingly, mutation of the other palmitoylation site C45 alone did not significantly diminish pyroptosis, but exacerbated attenuation of pyroptosis when combined with other cysteine mutations (Fig.4e, f, and Supplementary Fig.S4b). Given that C45 is located on the hydrophobic lipid-binding tip—a region masked by the

C-terminal domain in the full-length gasdermins and exposed after cleavage[17,19] (Fig.4b), we infer that C45 palmitoylation is auxiliary, amplifying membrane attachment in specific contexts rather than being strictly required for pore formation.

It has previously been reported that methylcobalamin (MeCbl) in a base-off conformation can coordinate Cys180 in GSDME and thereby prevent its recognition and cleavage by caspase-3[38]. To decouple the role of palmitoylation from caspase-3 mediated activation, we therefore examined caspase-3 processing of mammalian cell–expressed full-length GSDME and the C45A and C180A mutants, Cleavage efficiencies were comparable across all variants, indicating that palmitoylation at C45 or C180 does not affect caspase-3 cleavage (Supplementary Fig.S4c). We then directly compared pore-forming activity of palmitoylated versus non-palmitoylated GSDME using liposome-leakage assays with mammalian cell–expressed GSDME (palmitoylated), the cysteine mutants, and *E. coli*–expressed GSDME (non-palmitoylated). As expected, mammalian cell–expressed palmitoylated GSDME exhibited the strongest activity; C45A showed similar but delayed liposome leakage kinetics; C180A displayed a more pronounced reduction; the C45A/C180A double mutant and the *E. coli*–derived, non-palmitoylated GSDME were least active under matched conditions (Supplementary Fig.S4d). Together, these results establish that palmitoylation enhances GSDME pore-forming efficiency, with C180 as the primary functional site and C45 providing context-dependent augmentation.

Discussion

This study provides a comprehensive structural and mechanistic framework for understanding the cleavage and pore-formation of GSDME, a gasdermin family member increasingly implicated in cancer and inflammatory diseases. By determining cryo-EM structures of GSDME pores and performing systematic structure-function analysis, we uncover both the shared principles that

underpin the general mechanism of pore formation within GSDM family, and distinct features that distinguish GSDME from other gasdermins.

GSDME assembles into large, symmetrical β-barrel pores with 27- and 28-fold oligomeric states, similar to other characterized gasdermin pores. However, comparison of GSDME with other gasdermin pores quantitative variations in transmembrane β-barrel length and in the relative orientation between the globular “palm” domain and the membrane-inserting β-hairpin “fingers”. These geometric differences are expected to alter the extent and geometry of protein-membrane interfaces across gasdermins, with GSDMD, GSDMA3, GSDMB, and GSDME exhibiting progressively smaller predicted interface areas. Consistent with this structural diversity, gasdermins—while sharing conserved lipid-binding features—display distinct lipid preferences. For example, GSDMD binds strongly to phosphoinositides, cardiolipin, and phosphatidylserine[16,17], whereas GSDMB shows higher affinity for cardiolipin and bacterial lipids but reduced interaction with phosphatidylserine[39,40]. GSDME, interestingly, has been reported to preferentially target mitochondrial membranes rather than plasma membrane in neuron[41]. These observations suggest that differences in membrane-engagement geometry among gasdermins may tune membrane selectivity, enabling engagement of membranes with distinct biophysical properties, such as those of mitochondria versus the plasma membrane. Indeed, cardiolipin-rich mitochondrial membranes differ from the plasma membrane not only in lipid composition but also in surface charge density, curvature stress, and acyl-chain packing, and may present a modestly increased effective hydrophobic core thickness[42,43]. These features may enhance protein-lipid interactions and stabilize insertion of longer or more rigid transmembrane elements. In this context, the relatively long transmembrane β-barrel observed in GSDME (~40 Å) may be energetically more compatible with cardiolipin-enriched membranes. On the other hand, GSDME pore adopts a comparatively compact palm-finger geometry, which may influence the magnitude or steepness of concave membrane deformation induced by pore insertion[18]. Given that the ESCRT-III

membrane repair machinery preferentially assembles on curved membranes[18,44-46], variation in curvature magnitude could, in principle, modulate ESCRT-III filament organization and downstream membrane dynamics[47,48]

Unlike lipid-binding sites, which are highly conserved in specific residues, the oligomerization interfaces in GSDM pores are only structurally conserved but varied in their amino acid composition. This divergence likely serves an important biological function by preventing the formation of mixed or hetero-oligomeric pores among different gasdermin family members. Such specificity would be particularly important during complex cellular events, such as pathogen infection, where multiple gasdermins may be activated concurrently[49]. The lack of inter-gasdermin compatibility at the oligomerization interface ensures that each gasdermin functions independently, without interference or competition from other family members. Indeed, there is no evidence to date showing the existence of hetero-oligomeric gasdermin pores, except the gasdermin-like proteins in *Neurospora crassa*, which are activated through a distinct mechanism[50]. On the other hand, the amino acid divergence at the pore oligomerization interfaces presents a significant challenge in predicting pore stoichiometry or assessing whether a given gasdermin is capable of forming pores. Given that the pyroptotic activity of gasdermins is regulated by multiple factors, including but not limited to proteolytic cleavage and regulatory posttranslational modifications, functional assessment of gasdermins therefore requires a multifactorial approach that integrates structural, biochemical, and cellular analysis.

Our biochemical characterization of GSDME cleavage by caspase-3 reveals a distinct mode of activation. Unlike GSDMD, which requires dual-site engagement by inflammatory caspases involving both the recognition of a cleavage motif and additional interactions with a C-terminal exosite[35,36], GSDME is cleaved by caspase-3 solely through recognition of a tetrapeptide motif (DMPD) within the interdomain linker, independent of the C-terminal domain. This minimal recognition requirement likely enables GSDME to respond more rapidly to apoptotic signals, thus

facilitating the conversion of apoptosis into pyroptosis. It has to be mentioned that caspase-3 and -7 share a conserved recognition motif, however, only caspase-3 is capable of cleaving GSDME[8]. A recent study demonstrated that it is the GSDME C-terminal domain and the caspase-7 p10 subunit that determined the cleavability of GSDME by caspase-7[51], suggesting that caspase-7 may require additional substrate contacts beyond the cleavage motif. We therefore speculate that caspase-3 and caspase-7 may employ distinct substrate recognition strategies: caspase-3 cleaves substrates based primarily on motif recognition, whereas caspase-7 requires dual-site engagement. This hypothesis aligns well with the broader substrate specificity observed for caspase-3 than for caspase-7[52].

GSDME is *S*-palmitoylated at multiple cysteines in both its N- and C-terminal domains[22,37]. In this study, we identify palmitoylation at C180 within the GSDME-NT as a critical posttranslational modification that enhance its pyroptotic activity. Although C180 is not strictly conserved to C191 in GSDMD, it is similarly located within the transmembrane region in GSDME, suggesting that palmitoylation of this cysteine likely enhances the pyroptotic activity of GSDME by promoting membrane association and insertion. Surprisingly, C45 is also found to be palmitoylated in GSDME, but its modification, on its own, appears dispensable for pyroptotic activity but becomes relevant with palmitoylations of additional cystines, suggesting that C45 may play a modulatory role under specific cellular conditions. Taken together, our results support a multi-layered regulatory model for GSDME pore formation. Caspase-3-mediated cleavage is required to activate GSDME by releasing the pore-forming N-terminal domain, while *S*-palmitoylation acts as an additional regulatory input that fine-tunes its pyroptotic activity. Presenting these processes together provides a unified framework for understanding how GSDME activity is tightly controlled in cells.

In conclusion, our study provides the necessary structural blueprint of the human GSDME pore and elucidates the molecular mechanisms by which GSDME engages membranes,

oligomerizes, and is regulated by caspase cleavage and palmitoylation. These structural insights provide a molecular framework for future investigations into how pyroptotic signaling mediated by GSDME may be regulated in disease settings.

Methods

Constructs and Mutagenesis

The coding sequences of full-length human GSDMA, GSDMD and GSDME were synthesized at Twist Bioscience and cloned into a pET28-His-SUMO vector after the N-terminal His_6-SUMO tag and into a pDB-His-MBP vector with a N-terminal His_6-MBP tag. Caspase-3 (29–277) and caspase-11 (96–373) was cloned into a pET-22b vector for expression of the active form p17/p12 and p20/p10 complex. For the cellular experiments, full-length and N-terminal fragments of GSDMs were cloned into a pcDNA3.1 vector with a C-terminal FLAG-tag. The enzymatically inactive caspase-3 mutant ($p17^{C163A}$/p12) was generated by inserting $p17^{C163A}$ and p12 as individual ORFs into a single pET-22b vector under the control of the same lac operon. All mutations in this study were introduced using the QuikChange Site-Directed Mutagenesis Kit (Stratagene) or Gibson Assembly Master Mix (New England BioLabs), and all plasmids were verified by sequencing.

Expression and purification of GSDM proteins in *E. coli* and Expi293 cells

For protein expression in *E. coli,* BL21 (DE3) cells harboring the corresponding plasmids were grown in LB medium supplemented with 50 µg/mL kanamycin or 100 µg/mL ampicillin at 37 °C. Protein expression was induced by adding 0.5 mM Isopropyl β-D-1-thiogalactopyranoside (IPTG) at 20°C for 16 h when the OD_{600} reached 0.8. The cells were collected by centrifugation at 5,000× g for 20 min. The harvested cells were lysed by sonication (2 s on, 2 s off, 10 min total on, 40% power) in a buffer A containing 25 mM Tris-HCl at pH 8.0, 150 mM NaCl, 2 mM β-mercaptoethanol, and 25 mM imidazole. The lysates were centrifuged at 18,000× g at 4°C for 30 min to remove

insoluble fractions. Supernatants containing recombinant proteins were purified using Ni-NTA agarose (Qiagen) according to the manufacturer's instructions. For His_6-SUMO tagged GSDMs, the tag was removed on the Ni-NTA column at 4°C overnight with the addition of the home-made recombinant Ulp1. The flow-through non-tagged proteins were further purified with a Hitrap Q HP ion-exchange column (Cytiva) followed by a Superdex increase 200 (10/300) size exclusion column (Cytiva) in a buffer containing 25 mM HEPES at pH7.5 and 150 mM NaCl. All purified proteins were confirmed by Coomassie blue staining of SDS-PAGE.

For protein expression in mammalian cells, the Strep-tagged full length GSDME WT or indicated mutant constructs were transfected into Expi293 cells that were maintained in 500 ml serum-free SMM 293-TII Expression Medium (SinoBiological) and grown to 2.5×10^6 cells per ml, using polyethylenimine (PEI, Polysciences). The cells were fed with 10 mM sodium butyrate and 10 ml 45% d-(+)-glucose solution 12 h after transfection. The cells were grown for another 3 days and collected by centrifugation at 4,000× g for 30 min. The cell pellet was resuspended in buffer containing 40 mM HEPES at pH7.5, 150 mM NaCl, supplemented with protease inhibitor cocktail (Roche) and lysed by sonication (2 s on, 8 s off, 6 min total on, 35% power), and centrifuged at 40,000× g for 1 h. The supernatant was collected and incubated with Strep-Tactin®XT 4Flow agarose resin (IBA-lifesciences, 2-5030) for 3 h at 4 °C with gentle rotation. After washing, the protein was eluted using buffer A containing 50 mM biotin (Sigma-Aldrich). The eluted GSDME protein was snap-frozen for other assays. To obtain highly palmitoylated GSDME, AMA (Sigma-Aldrich, A8674) at 10 μg/ml was used to treat Expi293 cells for 4 h before collection.

Expression and purification of active caspases

Expression and purification of the constitutive-active caspase-3(p17/p12) or caspase-11(p20/p10) were performed as previously described[53,54]. Briefly, cDNA encoding the catalytic p30 domain of caspase-3 or caspase-11 was cloned into the pET22b vector, with a C-terminal 6×His tag fused to the p10 subunit. Recombinant proteins were expressed in *E.coli* following induction with 1 mM

IPTG for 20 h at 20 °C. During expression, the p30 precursor underwent autoproteolytic processing to generate the large and small catalytic subunits. Proteins were first purified by Ni-NTA affinity chromatography and subsequently subjected to size-exclusion chromatography using a Superdex 200 column. Purified caspases were concentrated, snap-frozen in liquid nitrogen, and stored at −80 °C for subsequent cleavage assays.

In vitro cleavage by active caspases

For cleavage by active caspase-3p17/p12 or caspase-11p20/p10, purified recombinant MBP tagged GSDME or indicated construct was incubated with purified active caspase-3 or -11 at a molar ratio of 10:1 in a 25-µl reaction containing 50 mM HEPES (pH 7.5), 3 mM EDTA, 150 mM NaCl. The reaction was incubated for 2 h at room temperature. Protein cleavage was examined by Coomassie blue staining of the reaction samples separated on the SDS–PAGE gel.

Liposome leakage assay

The liposome leakage assay was performed following an established protocol[20]. Briefly, 1-palmitoyl-2-oleoyl-sn-glycero-3-phosphocholine (PC) and cardiolipin (CL), or PC and 1,2-di-(9Z-octadecenoyl)-sn-glycero-3-phospho-L-serine (PS) (Avanti Polar Lipids), were mixed at molar ratios of 1:1 or 4:1, respectively, in a glass tube. The solvent chloroform was evaporated under a stream of nitrogen gas for 30 min. The dry lipid film was then rehydrated with Buffer B (25 mM HEPES at pH 7.5, 150 mM NaCl) supplemented with 50 mM 6-Carboxyfluorescein (6-FAM, Tokyo Chemical Industry Co., Ltd.). 6-FAM-loaded liposomes were then extruded through a 1 µm membrane (Whatman Nuclepore) using a mini-extruder (Avanti Polar Lipids). To remove the unencapsulated 6-FAM, the extruded liposomes were subjected to a PD-10 desalting column (Cytiva) equilibrated with Buffer B. For liposome leakage assay, liposomes were incubated with the GSDME in the absence or presence of caspase-3 p20/p10. Reactions were performed on a 384-well plate and the release of the 6-FAM dye was monitored by fluorescence at 517 nm using

a SpectraMax M5 plate reader (Molecular Devices), with excitation at 495 nm, for 60 min at 1-min intervals.

Isothermal titration calorimetry assay

Protein concentrations of full-length GSDME and inactive caspase-3 p20/p10C163A were measured in triplicate using a NanoDrop™ One Microvolume UV-Vis Spectrophotometer (Thermo Fisher Scientific) based on their extinction coefficients. Isothermal titration calorimetry measurements were performed at 20°C using a VP-ITC microcalorimeter (MicroCal Inc.). Experiments were performed by injecting 250 µL of caspase-3 solution (200 µM) into a sample cell containing 2 mL GSDME (50 µM) in 25 mM Tris-HCl at pH 8.0, 150 mM NaCl. A total of 25 injections were performed with a spacing of 300 s. All ITC data were analyzed using Origin Software provided by the manufacturer and fitted to a one-site binding model.

Cell culture and transfection

293T cells were obtained from the American Type Culture Collection (ATCC). The cells are frequently checked by virtue of their morphological features and functionalities. Cells were grown in Dulbecco's Modified Eagle medium (DMEM) supplemented with 10% (v/v) fetal bovine serum (FBS) and 2 mM L-glutamine at 37 °C in a 5% CO_2 incubator. Transient transfection in 293T cells was performed using the Lipofectamine 3000 (Thermo Fisher Scientific) following the manufacturers' instructions.

Cytotoxicity assay

Cell death was determined by Hoechst/propidium iodide (PI) double staining assay. 150 ng of indicated pcDNA-FLAG-GSDME construct (FL, NT, or indicated mutants) was transfected into HEK293T cells seeded in a 96-well plate at 2 x10^4 cells per well, respectively. Transfected cells were then cultured up to 40 h. At the start of assay, cells were stained with 30 µM propidium

iodide (Sigma Aldrich) for 10 min followed by 15 μM Hoechst 33342 (Thermo Fisher Scientific) for 15 min at 37°C in the dark. Afterward, cells were visualized under ZOE™ Fluorescent Cell Imager (Bio-Rad). Cell death was quantified and expressed as the percentage of PI positive cells to total cells (Hoechst-stained cells).

Metabolic labelling and detection of GSDME palmitoylation by click chemistry

Flag-tagged GSDME-NT was expressed in HEK293T cells by transfection with a pcDNA plasmid. Two hours after transfection, cells were treated with Alk-14 alkyne–palmitic acid (40 μM; Cayman Chemical, cat. no. 13266) for an additional 14 h in medium containing 10% charcoal-stripped FBS (Thermo Fisher Scientific, cat. no. A3382101). Cells were harvested by centrifugation at 4,000× g for 15 min and washed three times with PBS. Cell pellets were resuspended in lysis buffer containing 40 mM HEPES at pH 7.5, 150 mM NaCl, protease inhibitor cocktail, and 1% DDM, followed by sonication. Lysates were clarified by centrifugation at 15,000× g for 30 min. The supernatants were incubated with anti-FLAG magnetic beads (Sigma-Aldrich, cat. no. M8823) for 3 h at 4°C. Beads were washed three times with lysis buffer.

The bead-bound proteins were then subjected to a copper-catalyzed click chemistry assay using a commercial detection kit (Badrilla, cat. no. K010-410). Briefly, the beads were incubated in the provided buffer for 15 min, followed by the addition of the click reaction mixture containing TAMRA-azide as the fluorescent reporter (Lumiprobe, cat. no. B7130), along with the catalytic, stabilizer, and activator reagents. The reaction was incubated for 1 h at room temperature on a rotary wheel. After completion of the click reaction, the samples were divided into two aliquots and pelleted. Each aliquot was resuspended in 30 μl of 1× SDS-Laemmli sample buffer, with or without β-mercaptoethanol, and boiled for 5 min. Proteins were resolved by SDS-PAGE, and *S*-Palmitoylated GSDME was visualized directly in the gel by detecting rhodamine fluorescence using a ChemiDoc MP imaging system. The gel was subsequently processed for Western blotting

and probed with anti-GSDME (Cell Signaling Technology, cat. no. E2X7E) and anti-FLAG antibodies (Sigma-Aldrich, cat. no. F1804).

Detection of GSDME palmitoylation by the RapidSPALM kit

The assay was basically following the protocol provided by the RapidSPALM Protein S-Palmitoylation Detection Kit (BioDynamics Laboratory Inc., F017A). Briefly, HEK293T cells transfected with GSDME WT or its mutant plasmids from 6-well plate were scraped and following collected by centrifugation at 400× g for 5 minutes. The cell pellet was gently washed twice with cold PBS and resuspended in 300 µL of 1× Basal Buffer (50 mM sodium phosphate at pH 7.4, 100 mM NaCl, 2% SDS) provided in the kit. Cells were lysed by sonication using a 2-second on/off cycle for 5 cycles at 10% power. Cell lysates were centrifuged at 20,000× g for 10 minutes, and the supernatant was collected. Protein concentration was determined using the BCA Protein Assay Kit (Thermo Fisher, 23225), and the lysate was diluted to 1 mg/mL for the following reactions. Palmitoyl-MfTag Exchange was performed following manufacturer's protocol. After the exchange reaction, protein samples were purified via chloroform/methanol precipitation to remove non-protein biomolecules. The resulting protein pellets were dried and resuspended in 25 µL of 1× Basal Buffer followed by a water-bath sonication. All the samples were subjected to SDS-PAGE followed by western blotting analysis using an anti-Flag antibody (Sigma-Aldrich).

GSDME pore reconstitution and purification.

Purified GSDME was added to the prepared liposomes, followed by the addition of active caspase-3 p17/p12 to initiate pore formation. The reaction was incubated on ice for 3 h. After that, the liposomes loaded with GSDME pores were solubilized by 2% C12E8 (Anatrace) to extract the pores. To remove poorly behaving particles and GSDME-CT, the samples were further purified using a Superose 6 (10/300) Increase size exclusion column (Cytiva) equilibrated with Buffer B (25 mM HEPES at pH 7.5, 150 mM NaCl, and 0.006% C12E8).

Negative staining electron microscopy

For negative staining, 10 µL of the GSDME pore was applied onto a glow-discharged carbon-coated copper grid (Electron Microscopy Sciences). The sample was incubated on grid for 1 min, stained with 1% uranyl acetate for 1 min, and blotted dry. The grids were imaged on the Hitachi H-7650 transmission electron microscope equipped with a 2k CCD camera (Advanced Microscopy Techniques) at the UCONN Health Electron Microscopy Facility.

Cryo-EM grid preparation and data acquisition

3.5 µL of the freshly purified GSDME pores at 2 mg/mL was applied to plasma glow discharged, Quantifoil holey copper grids (R 1.2/1.3, 400 mesh, Electron Microscopy Sciences), using a Vitrobot Mark IV (Thermo Fisher Scientific) set at blotting force 4, blotting time 5.5 s, 100% humidity, and 4°C. Blotted grids were immediately plunged into liquid ethane and transferred to liquid nitrogen for storage. Cryo-EM data were collected at the Laboratory of Biological Electron Microscopy at Ecole Polytechnique Fédérale de Lausanne (EPFL) in Switzerland using the automated data acquisition software EPU (TFS) on Titan Krios G4 transmission electron microscope (TFS), operating at 300 kV and equipped with cold field-emission gun electron sources and either a Falcon4i direct detection camera. Datasets were recorded in counting mode at a physical pixel size of 0.926 Å and a defocus range of 0.8 to 2.5 µm with a total electron dose of 50 e− / $Å^2$. Image data were saved as Electron Event Recordings.

Cryo-EM image processing

Raw movies were corrected by gain reference and for beam-induced motion and summed into motion-corrected images using MotionCor2[55]. Contrast transfer function (CTF) parameters were determined using CTFFind4[56] and refined later in cryoSPARC[57].

A subset of 500 micrographs were subject to manual picking with particles used to train a Topaz model[58] in cryoSPARC, which was subsequently use to pick 129,042 particles from 10,552 micrographs. 2D classification was performed in cryoSPARC to eliminate ice, carbon edges, and false-positive particles containing noise. Three rounds of 2D classification were conducted, yielding 95,547 particles. An *ab*-initial model was generated de novo in cryoSPARC using these particles. 3D classification with C1 symmetry was performed, yielding a class of 27-fold GSDME pore containing 17,305 particles, a class of 28-fold GSDME pore containing 44,334 particles, and other class of pores with uncertain symmetries. The 27- abd 28-fold GSDME pore particles were then selected for non-uniform refinement in cryoSPARC with appropricate symmetries, yielding the final 3D reconstruction of 27-fold GSDME pore at an over resolution of 3.64 Å and the 28-fold GSDME pore at 3.58 Å resolution, measured by the gold standard Fourier shell correlation (FSC) = 0.143 criteria.

Model building and structure analysis

Atomic models of GSDME pore were built and refined into the cryo-EM density using Coot[59] and PHENIX[60]. An AlphaFold2-predicted monomeric GSDME model (UniProt O60443, AF-O60443-F1-v4) was used as an initial reference for model building[61]; all oligomeric and membrane-inserted features were built and refined against the cryo-EM density. Model of the GSDME N-terminal domain was first docked into the EM density as a rigid body in Chimera[62], then manually adjusted in Coot. The structural model of the complex was further refined using the phenix.real_space_refine with secondary structure restraints and Coot iteratively. The quality of the atomic model was evaluated using the Molprobity[63]. Figures were prepared using PyMOL (The PyMOL Molecular Graphics System, Version 2.0, Schrödinger, LLC.) and UCSF Chimera.

Statistical & Reproducibility

All experiments were repeated at least three times unless specified. Analysis was performed using the statistical package GraphPadPrism 10.

Data availability

The atomic coordinates of the 27- and 28-fold GSDME pores have been deposited in the Protein Data Bank (PDB) under accession numbers 9PE0 [https://doi.org/10.2210/pdb9pe0/pdb] and 9PDU [https://doi.org/10.2210/pdb9pdu/pdb], respectively. The associated cryo-EM density maps have been deposited in the Electron Microscopy Data Bank (EMDB) under accession numbers EMD-71549 [https://www.ebi.ac.uk/emdb/EMD-71549] and EMD-71544 [https://www.ebi.ac.uk/emdb/EMD-71544], respectively. All other data are available from the corresponding author upon request. Several structural coordinates in the PDB database were used in this study, which can be located by accession numbers 6CB8 [https://doi.org/10.2210/pdb6cb8/pdb], 5B5R [https://doi.org/10.2210/pdb5b5r/pdb], 6N9O [https://doi.org/10.2210/pdb6n9o/pdb], 6N9N [https://doi.org/10.2210/pdb6n9n/pdb], 6VFE [https://doi.org/10.2210/pdb6vfe/pdb], 7V8H [https://doi.org/10.2210/pdb7v8h/pdb], and 3CVR [https://doi.org/10.2210/pdb3cvr/pdb]. The source data are provided as a Source Data file.

References

1. Shi, J., Gao, W. & Shao, F. Pyroptosis: Gasdermin-Mediated Programmed Necrotic Cell Death. *Trends Biochem Sci* **42**, 245-254 (2017).
2. Tan, Y. et al. Pyroptosis: a new paradigm of cell death for fighting against cancer. *J Exp Clin Cancer Res* **40**, 153 (2021).
3. Bai, Y., Pan, Y. & Liu, X. Mechanistic insights into gasdermin-mediated pyroptosis. *Nat Rev Mol Cell Biol* (2025).
4. Wang, C. & Ruan, J. Mechanistic Insights into Gasdermin Pore Formation and Regulation in Pyroptosis. *J Mol Biol* **434**, 167297 (2022).
5. Kayagaki, N. et al. Caspase-11 cleaves gasdermin D for non-canonical inflammasome signalling. *Nature* **526**, 666-71 (2015).

6. Shi, J. et al. Cleavage of GSDMD by inflammatory caspases determines pyroptotic cell death. *Nature* **526**, 660-5 (2015).
7. Rogers, C. et al. Cleavage of DFNA5 by caspase-3 during apoptosis mediates progression to secondary necrotic/pyroptotic cell death. *Nat Commun* **8**, 14128 (2017).
8. Wang, Y. et al. Chemotherapy drugs induce pyroptosis through caspase-3 cleavage of a gasdermin. *Nature* **547**, 99-103 (2017).
9. Orning, P. et al. Pathogen blockade of TAK1 triggers caspase-8-dependent cleavage of gasdermin D and cell death. *Science* **362**, 1064-1069 (2018).
10. Sollberger, G. et al. Gasdermin D plays a vital role in the generation of neutrophil extracellular traps. *Sci Immunol* **3**(2018).
11. Hou, J. et al. PD-L1-mediated gasdermin C expression switches apoptosis to pyroptosis in cancer cells and facilitates tumour necrosis. *Nat Cell Biol* **22**, 1264-1275 (2020).
12. Zhou, Z. et al. Granzyme A from cytotoxic lymphocytes cleaves GSDMB to trigger pyroptosis in target cells. *Science* **368**(2020).
13. Zhang, J.Y. et al. The metabolite alpha-KG induces GSDMC-dependent pyroptosis through death receptor 6-activated caspase-8. *Cell Res* **31**, 980-997 (2021).
14. Deng, W. et al. Streptococcal pyrogenic exotoxin B cleaves GSDMA and triggers pyroptosis. *Nature* **602**, 496-502 (2022).
15. Zhang, Z. et al. Gasdermin E suppresses tumour growth by activating anti-tumour immunity. *Nature* **579**, 415-420 (2020).
16. Liu, X. et al. Inflammasome-activated gasdermin D causes pyroptosis by forming membrane pores. *Nature* **535**, 153-8 (2016).
17. Ding, J. et al. Pore-forming activity and structural autoinhibition of the gasdermin family. *Nature* **535**, 111-6 (2016).
18. Xia, S. et al. Gasdermin D pore structure reveals preferential release of mature interleukin-1. *Nature* **593**, 607-611 (2021).
19. Ruan, J., Xia, S., Liu, X., Lieberman, J. & Wu, H. Cryo-EM structure of the gasdermin A3 membrane pore. *Nature* **557**, 62-67 (2018).
20. Wang, C. et al. Structural basis for GSDMB pore formation and its targeting by IpaH7.8. *Nature* **616**, 590-597 (2023).
21. Zhong, X. et al. Structural mechanisms for regulation of GSDMB pore-forming activity. *Nature* **616**, 598-605 (2023).
22. Du, G. et al. ROS-dependent S-palmitoylation activates cleaved and intact gasdermin D. *Nature* **630**, 437-446 (2024).
23. Balasubramanian, A. et al. The palmitoylation of gasdermin D directs its membrane translocation and pore formation during pyroptosis. *Sci Immunol* **9**, eadn1452 (2024).
24. Zhang, N. et al. A palmitoylation-depalmitoylation relay spatiotemporally controls GSDMD activation in pyroptosis. *Nat Cell Biol* **26**, 757-769 (2024).
25. Zhou, B. et al. Full-length GSDME mediates pyroptosis independent from cleavage. *Nat Cell Biol* **26**, 1545-1557 (2024).
26. Margheritis, E. et al. Gasdermin D cysteine residues synergistically control its palmitoylation-mediated membrane targeting and assembly. *EMBO J* **43**, 4274-4297 (2024).
27. Mulvihill, E. et al. Mechanism of membrane pore formation by human gasdermin-D. *EMBO J* **37**(2018).
28. Schaefer, S.L. & Hummer, G. Sublytic gasdermin-D pores captured in atomistic molecular simulations. *Elife* **11**(2022).
29. Sborgi, L. et al. GSDMD membrane pore formation constitutes the mechanism of pyroptotic cell death. *EMBO J* **35**, 1766-78 (2016).
30. Wright, S.S. et al. Transplantation of gasdermin pores by extracellular vesicles propagates pyroptosis to bystander cells. *Cell* **188**, 280-291 e17 (2025).

31. Kappelhoff, S. et al. Structure and regulation of GSDMD pores at the plasma membrane of pyroptotic cells. *bioRxiv*, 2023.10.24.563742 (2023).
32. Zhou, B. & Abbott, D.W. Gasdermin E permits interleukin-1 beta release in distinct sublytic and pyroptotic phases. *Cell Rep* **35**, 108998 (2021).
33. Kong, Q. et al. Alternative splicing of GSDMB modulates killer lymphocyte-triggered pyroptosis. *Sci Immunol* **8**, eadg3196 (2023).
34. Oltra, S.S. et al. Distinct GSDMB protein isoforms and protease cleavage processes differentially control pyroptotic cell death and mitochondrial damage in cancer cells. *Cell Death Differ* **30**, 1366-1381 (2023).
35. Wang, K. et al. Structural Mechanism for GSDMD Targeting by Autoprocessed Caspases in Pyroptosis. *Cell* **180**, 941-955 e20 (2020).
36. Liu, Z. et al. Caspase-1 Engages Full-Length Gasdermin D through Two Distinct Interfaces That Mediate Caspase Recruitment and Substrate Cleavage. *Immunity* **53**, 106-114 e5 (2020).
37. Hu, L. et al. Chemotherapy-induced pyroptosis is mediated by BAK/BAX-caspase-3-GSDME pathway and inhibited by 2-bromopalmitate. *Cell Death Dis* **11**, 281 (2020).
38. Xu, W. et al. Methylcobalamin protects against liver failure via engaging gasdermin E. *Nat Commun* **16**, 1233 (2025).
39. Hansen, J.M. et al. Pathogenic ubiquitination of GSDMB inhibits NK cell bactericidal functions. *Cell* **184**, 3178-3191 e18 (2021).
40. Chao, K.L., Kulakova, L. & Herzberg, O. Gene polymorphism linked to increased asthma and IBD risk alters gasdermin-B structure, a sulfatide and phosphoinositide binding protein. *Proc Natl Acad Sci U S A* **114**, E1128-E1137 (2017).
41. Neel, D.V. et al. Gasdermin-E mediates mitochondrial damage in axons and neurodegeneration. *Neuron* **111**, 1222-1240 e9 (2023).
42. Pan, J. et al. Structural and mechanical properties of cardiolipin lipid bilayers determined using neutron spin echo, small angle neutron and X-ray scattering, and molecular dynamics simulations. *Soft Matter* **11**, 130-8 (2015).
43. Wilson, B.A., Ramanathan, A. & Lopez, C.F. Cardiolipin-Dependent Properties of Model Mitochondrial Membranes from Molecular Simulations. *Biophys J* **117**, 429-444 (2019).
44. Ruhl, S. et al. ESCRT-dependent membrane repair negatively regulates pyroptosis downstream of GSDMD activation. *Science* **362**, 956-960 (2018).
45. Bertin, A. et al. Human ESCRT-III polymers assemble on positively curved membranes and induce helical membrane tube formation. *Nat Commun* **11**, 2663 (2020).
46. Lee, I.H., Kai, H., Carlson, L.A., Groves, J.T. & Hurley, J.H. Negative membrane curvature catalyzes nucleation of endosomal sorting complex required for transport (ESCRT)-III assembly. *Proc Natl Acad Sci U S A* **112**, 15892-7 (2015).
47. Zhu, Y. et al. NINJ1 regulates plasma membrane fragility under mechanical strain. *Nature* **644**, 1088-1096 (2025).
48. Kayagaki, N. et al. NINJ1 mediates plasma membrane rupture during lytic cell death. *Nature* **591**, 131-136 (2021).
49. Wright, S.S. et al. A bacterial toxin co-opts caspase-3 to disable active gasdermin D and limit macrophage pyroptosis. *Cell Rep* **43**, 114004 (2024).
50. Li, Y. et al. Cleavage-independent activation of ancient eukaryotic gasdermins and structural mechanisms. *Science* **384**, adm9190 (2024).
51. Xu, H., Yuan, Z., Qin, K., Jiang, S. & Sun, L. The molecular mechanism and evolutionary divergence of caspase 3/7-regulated gasdermin E activation. *Elife* **12**(2024).
52. Walsh, J.G. et al. Executioner caspase-3 and caspase-7 are functionally distinct proteases. *Proc Natl Acad Sci U S A* **105**, 12815-9 (2008).
53. Wang, C. et al. LPS-induced structural reorganization and polymerization drive noncanonical inflammasome activation. *Sci Adv* **12**, eadz4623 (2026).

54. Hwang, D., Kim, S.A., Yang, E.G., Song, H.K. & Chung, H.S. A facile method to prepare large quantities of active caspase-3 overexpressed by auto-induction in the C41(DE3) strain. *Protein Expr Purif* **126**, 104-108 (2016).
55. Zheng, S.Q. et al. MotionCor2: anisotropic correction of beam-induced motion for improved cryo-electron microscopy. *Nat Methods* **14**, 331-332 (2017).
56. Rohou, A. & Grigorieff, N. CTFFIND4: Fast and accurate defocus estimation from electron micrographs. *J Struct Biol* **192**, 216-21 (2015).
57. Punjani, A., Rubinstein, J.L., Fleet, D.J. & Brubaker, M.A. cryoSPARC: algorithms for rapid unsupervised cryo-EM structure determination. *Nat Methods* **14**, 290-296 (2017).
58. Bepler, T. et al. Positive-unlabeled convolutional neural networks for particle picking in cryo-electron micrographs. *Nat Methods* **16**, 1153-1160 (2019).
59. Emsley, P., Lohkamp, B., Scott, W.G. & Cowtan, K. Features and development of Coot. *Acta Crystallogr D Biol Crystallogr* **66**, 486-501 (2010).
60. Adams, P.D. et al. PHENIX: a comprehensive Python-based system for macromolecular structure solution. *Acta Crystallogr D Biol Crystallogr* **66**, 213-21 (2010).
61. Jumper, J. et al. Highly accurate protein structure prediction with AlphaFold. *Nature* **596**, 583-589 (2021).
62. Pettersen, E.F. et al. UCSF Chimera--a visualization system for exploratory research and analysis. *J Comput Chem* **25**, 1605-12 (2004).
63. Chen, V.B. et al. MolProbity: all-atom structure validation for macromolecular crystallography. *Acta Crystallogr D Biol Crystallogr* **66**, 12-21 (2010).

Acknowledgments

This work was supported by UConn Health Start-up fund and US National Institutes of Health grants R01AI158435 to J.R.

Author Contributions Statement

J.R. conceived the study. E.T. expressed and purified the proteins. E.T. and J.R. reconstituted the GSDME pores. C.W. froze the cryo-EM grids. J.W. and D.N. screened and collected the cryo-EM datasets. J.R. and D.N. processed the cryo-EM datasets. J.R. built the atomic model. J.R. T.T., and E.T. analyzed the structures and performed biochemical experiments. T.T., C.W., E.T., and X.W. performed cellular experiments. J.R. and V.R. supervised cellular experiments and analyzed the data. All authors organized and analyzed data. J.R. wrote the paper with input from all authors.

Competing Interests Statement

The authors declare no competing interests.

Figure Legends

Fig.1: Cryo-EM structure of the human GSDME pore and structural comparison of with other GSDM pores. a, Ribbon diagram and dimensions of the 28-subunit human GSDME pore structure fitted into its cryo-EM density. The pore features a large transmembrane β-barrel and a globular domain on the cytosolic side. **b**, Electrostatic surface potential map of the GSDME pore (−5 to +5 kT/e) of the GSDME pore, highlighting the acidic acidic conduit. **c**, Structure of a pore-form GSDME-NT protomer shown with a transparent surface overlay. The structure resembles a human left hand, with the globular domain as the 'palm', the α1 helix as the 'thumb', the membrane-inserted β-hairpins as the 'fingers' and the β1-β2 loop as the 'wrist'. **d**, Structural comparison of the transmembrane β-barrel regions among human GSDME, mouse GSDMA3, human GSDMB, and human GSDMD pores. Structures are aligned by the α1 helix. The traversing distance across the lipid bilayer in each pore was measured from the α1 helix to the tip of the β-hairpins. A.A., amino acid. **e**, Comparison of the junction between the globular domain and β-barrel among GSDM pores. Structures were aligned based on the β-barrel and α1 helix. GSDME exhibits the comparatively compact conformation, with its globular domain positioned closest to the membrane surface relative to other gasdermins.

Fig.2: Mechanism of lipid binding and oligomerization of GSDME pore. a, Lipid binding sites in GSDME are shown as electrostatic potential surface (upper panel) and key residues are highlighted and shown as balls and sticks (lower panel). **b** and **c**, Impairment of the pore-forming ability of GSDME by mutations in the lipid binding sites, shown by liposome leakage assay (n = 3 biological replicates, Error bars, mean ± SD). FL, full-length; N+C, cleaved by caspase-3p17p12; WT, wild-type; BS1, K4E/R7E/R11E; BS2: K41E/R42E/R47E/K50E; Anchor2G, F43G/W44G/W46G; Anchor2E, F43E/W44E/W46E. **d**, Pyroptotic cell death of HEK293T cells

expressing wild-type or indicated GSDME-NT mutant, monitored by Hoechst/Propidium iodide (PI) double-staining. Error bars, mean ± SD of 3 biological replicates. Immunoblot analysis of GSDME-NT expression with an anti-FLAG antibody is shown below, with β-actin as a loading control, indicating no less expression of mutants than wild-type. **e**, Lipid binding site 4 (BS4) in GSDME. Key residues in BS4 are shown as balls and sticks. BS1–3 are colored blue and the C-terminus of the GSDME-NT is colored orange. **f**, Impairment of the pore-forming ability of GSDME by mutations in BS4, shown by liposome leakage assay (n = 3 biological replicates, Error bars, mean ± SD). **g**, Two neighboring subunits in the GSDME pore are shown. Structural elements that participate in oligomerization are labeled and colored cyan. Two oligomerization interfaces (I and II) in globular domain are highlighted. C-terminus of the GSDME-NT is highlighted with a red dot. **h**, Detail views of Interface I (top panel) and II (bottom panel). **i**, Impairment of the pore-forming ability of GSDME by mutations in the oligomerization interfaces, shown by liposome leakage assay (n = 3 biological replicates, Error bars, mean ± SD).

Fig.3: Caspase-3 cleaves GSDME independently of the C-terminal domain. a, Size exclusion cryotomography analysis of GSDME, caspase-3p17p12, and GSDME incubated with caspase-3p17p12. The C163A inactive mutant of caspase-3p17p12 was used. **b**, Isothermal titration calorimetry (ITC)-based measurement of the binding affinities of caspase-3p17/p12 with full-length GSDME (left) and GSDME C-terminal domain (right), respectively. K_d, dissociation constant; DP, differential power measured by the ITC machine; ΔH, heat change measured by the ITC machine. The representative of three technical replicates (n=3) is shown. **c**, Schematic of wild type and engineered GSDME and GSDMA used for caspase-3/-11 cleavage. **d** and **e**, MBP tagged wild type GSDME, GSDMD, and engineered GSDME mutants were subjected for cleavage by active caspase-3p17p12 (**d**) and caspase-11p20p10 (**e**). Results are representative of at least three independent experiments. The cleaved products were analyzed by SDS–PAGE followed by Coomassie-blue staining. FL, full-length; NT, N-terminal fragment; CT, C-terminal

fragment. GSDMD can be cleaved by caspase-3 at D88. Products 1 and 2 are generated by the cleavage of chimeric GSDME mutants by caspase-11 at potential alternative cleavage sites. **f**, Alphafold predicted structure of full-length GSDME. There are multiple aspartic acid residues in flexible regions structural close to the caspase-3 cleavage site. **g**, Human GSDMA and an engineered GSDMA construct in which the GSDME interdomain linker motif "DMPD" was introduced ($GSDMA^{DMPD}$) were subjected for cleavage by active caspase-3p17p12. Results are representative of at least three independent experiments.

Fig.4: Palmitoylation regulates GSDME pore-forming activity. a, Non-reducing SDS–PAGE followed by in-gel fluorescence and immunoblot analysis of GSDME-NT expressed in HEK293T cells. Cells expressing GSDME-NT were metabolically labelled with palmitic acid alkyne supplemented in medium followed by copper-based click chemistry analysis with tetramethyl-rhodamine (TAMRA) azide. Samples were analyzed in the absence (–) or presence (+) of the reducing agent β-mercaptoethanol (β-ME). Results are representative of at least three independent experiments. **b**, Superposition of the structure of the pore-form GSDME-NT with the Alphafold predicted structure of the auto-inhibited full-length GSDME. The pore-form GSDME-NT is colored orange and the full-length GSDME is colored palecyan. Five cysteine residues in GSDME-NT are highlighted as red spheres and labeled. C180 is located on the β7 strand within the transmembrane region; C168 is situated at the junction between the globular and transmembrane domains. The remaining three cysteines reside in the globular subdomain, with C45 positioned at the β1-β2 tip and C156 buried and not surface-exposed. **c**, Schematic of the palmitoylation detection assay using the RapidSPALM kit. The kit detects S-palmitoyl/acyl modifications by converting them into a multifunctional tag (MfTag, ~5 kDa). hpHA, high performance hydroxylamine-derivative. **d**, Palmitoylation of Wild-type GSDME-NT and Cys mutants of GSDME-NT. Two palmitoylation sites were detected and the positions of singly (palm ×1) and doubly (palm ×2) palmitoylated species are indicated. C180A and C45A mutants altered

the palmitoylation signature. Results are representative of at least three independent experiments. **e**, Representative fluorescence microscopy images of HEK293T cells transiently transfected with indicated constructs of GSDME. Cells were stained with Hoechst 33342 and PI 24 hours post-transfection. **f**, Quantification of pyroptotic cell death induced by GSDME cysteine mutants in HEK293T cells, assessed by Hoechst/PI double-staining from (**e**). Data represent mean ± s.d. from three independent experiments with two technical replicates of each.

Gasdermins form membrane pores that drive inflammatory cell death. Here, authors determine high-resolution structures of human GSDME pores and show how caspase-3 cleavage and lipid modification together regulate pore assembly and activity.

Peer review information: *Nature Communications* thanks the anonymous reviewers for their contribution to the peer review of this work. A peer review file is available.

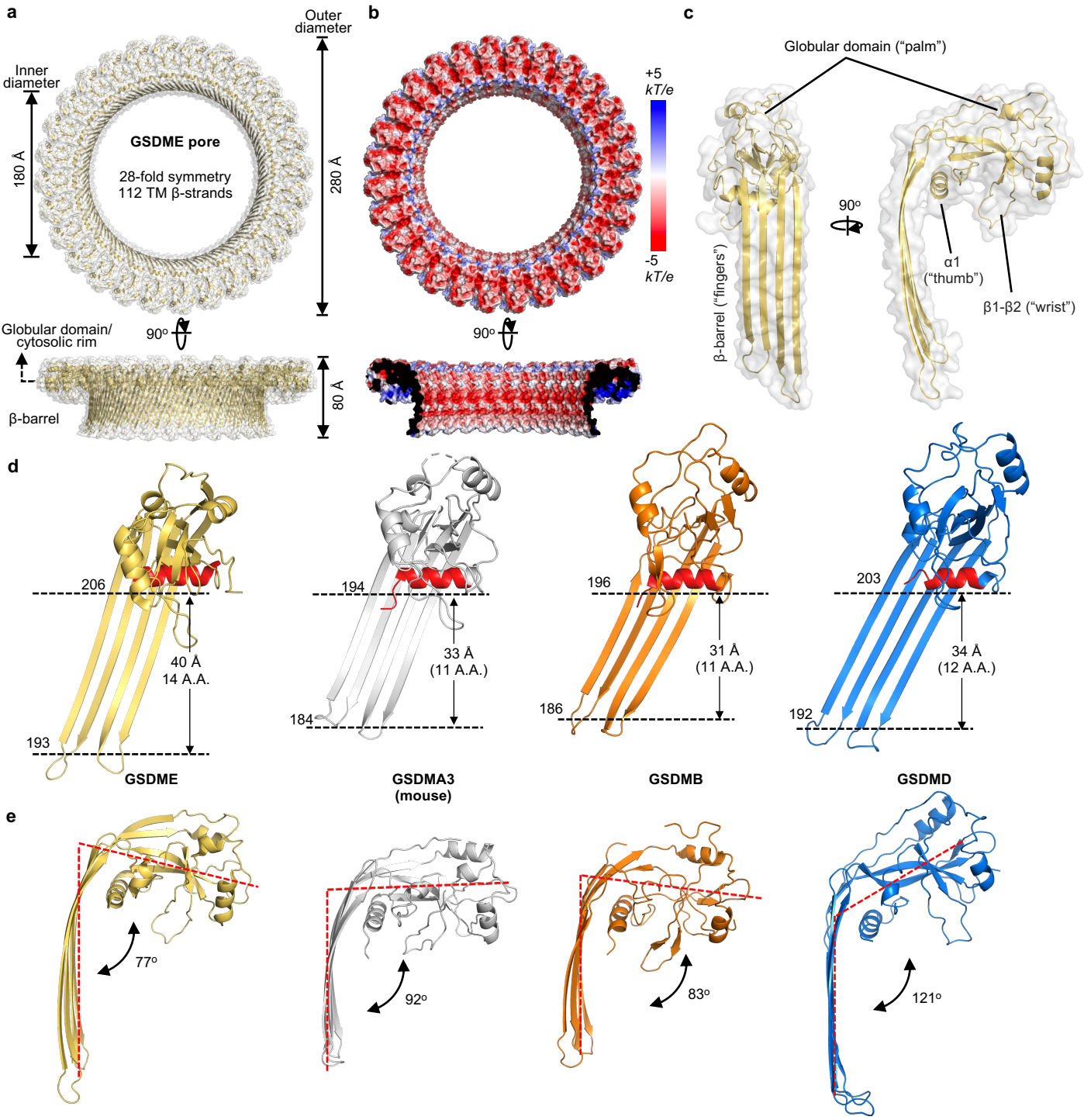
a
Inner diameter
180 Å
GSDME pore
28-fold symmetry
112 TM β-strands
Outer diameter
280 Å
Globular domain/ cytosolic rim
90°
β-barrel
80 Å
b
+5 kT/e
-5 kT/e
90°
c
Globular domain (“palm”)
90°
β-barrel (“fingers”)
α1 (“thumb”)
β1-β2 (“wrist”)
d
206
40 Å
14 A.A.
193
GSDME
194
33 Å
(11 A.A.)
184
GSDMA3 (mouse)
196
31 Å
(11 A.A.)
186
GSDMB
203
34 Å
(12 A.A.)
192
GSDMD
e
77°
92°
83°
121°

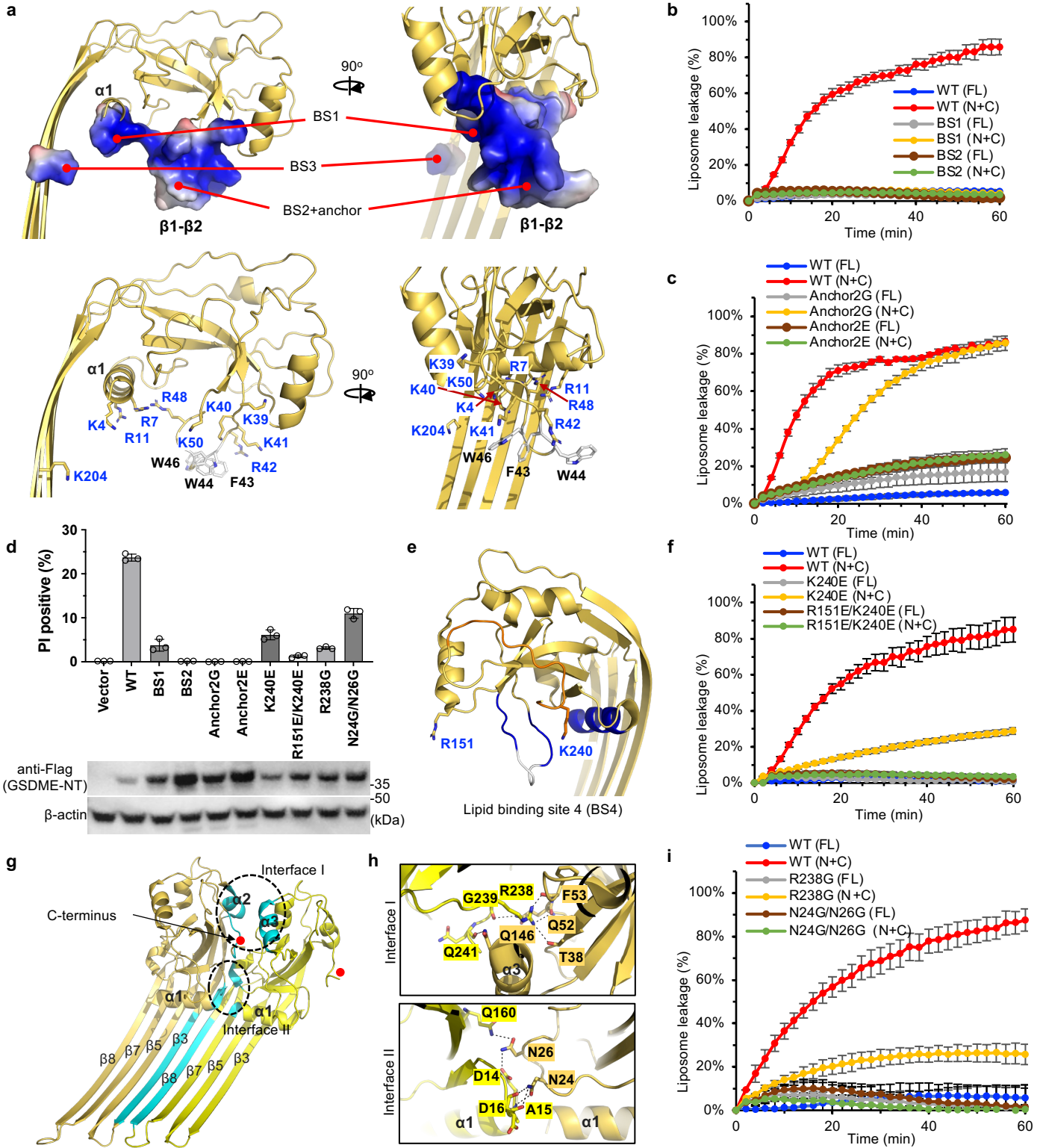
a
α1
BS1
BS3
BS2+anchor
β1-β2
90°
β1-β2
α1
K4
R48
R7
R11
K40
K39
K50
K41
W46
R42
W44
F43
K204
90°
K39
R7
K50
K40
R11
K4
R48
K204
K41
R42
W46
F43
W44
b
Liposome leakage (%)
Time (min)
WT (FL)
WT (N+C)
BS1 (FL)
BS1 (N+C)
BS2 (FL)
BS2 (N+C)
c
Liposome leakage (%)
Time (min)
WT (FL)
WT (N+C)
Anchor2G (FL)
Anchor2G (N+C)
Anchor2E (FL)
Anchor2E (N+C)
d
PI positive (%)
Vector
WT
BS1
BS2
Anchor2G
Anchor2E
K240E
R151E/K240E
R238G
N24G/N26G
anti-Flag
(GSDME-NT)
β-actin
-35
-50
(kDa)
e
R151
K240
Lipid binding site 4 (BS4)
f
Liposome leakage (%)
Time (min)
WT (FL)
WT (N+C)
K240E (FL)
K240E (N+C)
R151E/K240E (FL)
R151E/K240E (N+C)
g
Interface I
C-terminus
α2
α3
α1
α1
Interface II
β8
β7
β5
β3
β8
β7
β5
β3
h
Interface I
G239
R238
F53
Q52
Q146
Q241
T38
α3
Interface II
Q160
N26
D14
N24
D16
A15
α1
α1
i
Liposome leakage (%)
Time (min)
WT (FL)
WT (N+C)
R238G (FL)
R238G (N+C)
N24G/N26G (FL)
N24G/N26G (N+C)

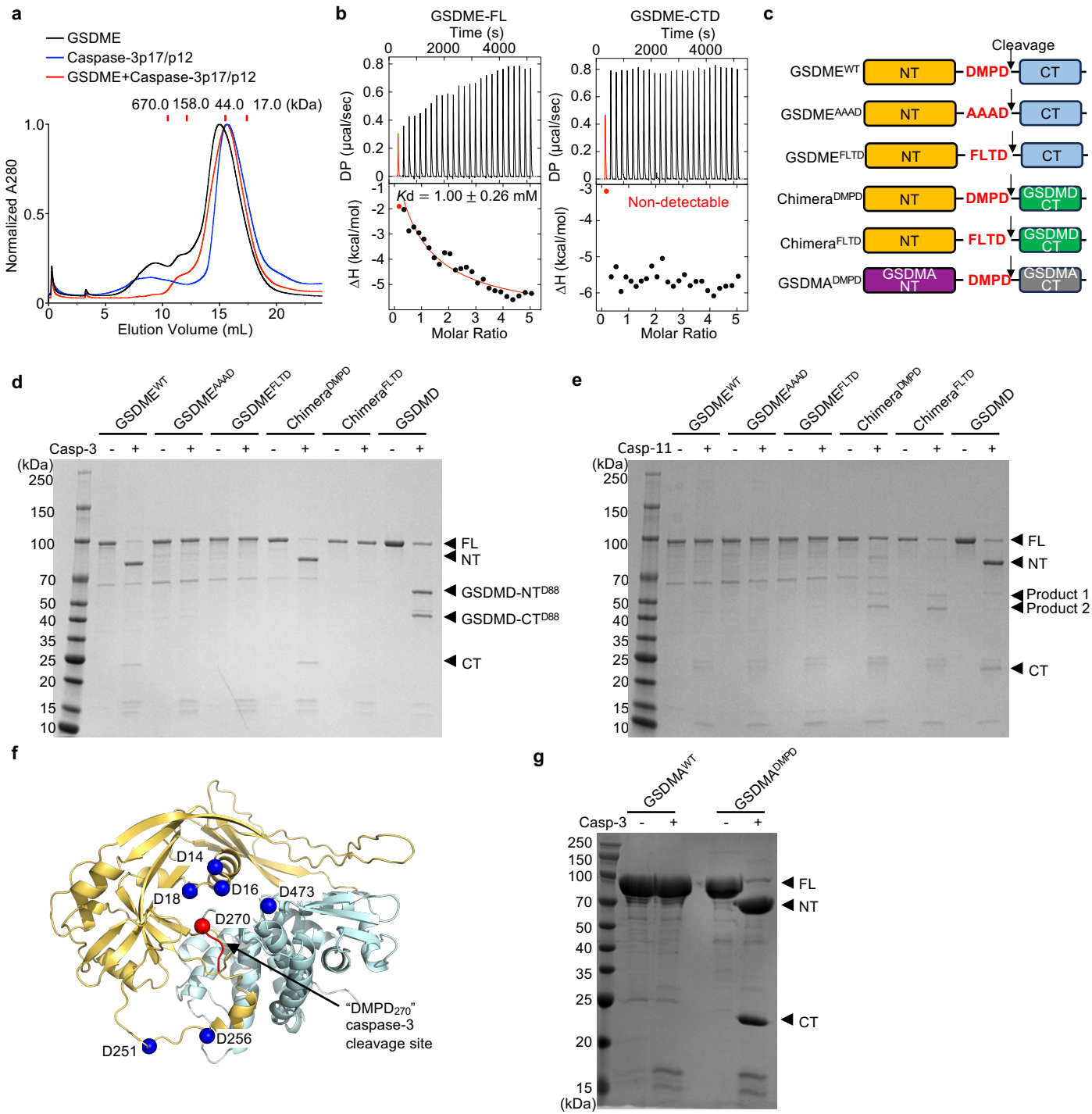
a
GSDME
Caspase-3p17/p12
GSDME+Caspase-3p17/p12
670.0 158.0 44.0 17.0 (kDa)
Normalized A280
Elution Volume (mL)
b
GSDME-FL
GSDME-CTD
Time (s)
DP (μcal/sec)
Kd = 1.00 ± 0.26 mM
Non-detectable
ΔH (kcal/mol)
Molar Ratio
c
Cleavage
GSDME^WT
GSDME^AAAD
GSDME^FLTD
Chimera^DMPD
Chimera^FLTD
GSDMA^DMPD
NT
CT
DMPD
AAAD
FLTD
GSDMD CT
GSDMA NT
GSDMA CT
d
GSDME^WT
GSDME^AAAD
GSDME^FLTD
Chimera^DMPD
Chimera^FLTD
GSDMD
Casp-3
(kDa)
FL
NT
GSDMD-NT^D88
GSDMD-CT^D88
CT
e
Casp-11
Product 1
Product 2
f
D14
D16
D18
D270
D473
D251
D256
"DMPD270" caspase-3 cleavage site
g
GSDMA^WT
GSDMA^DMPD
Casp-3

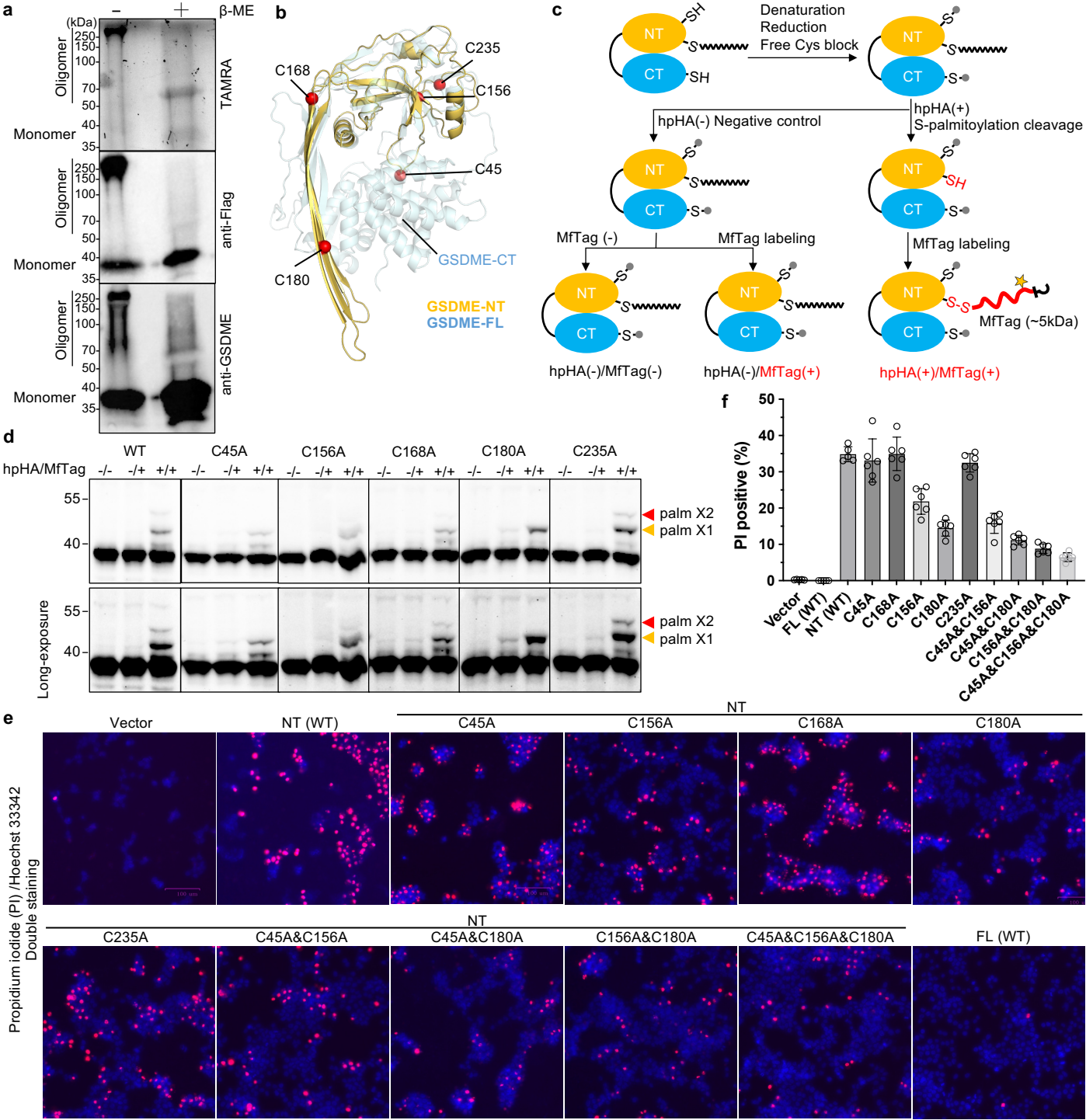
a
β-ME
(kDa)
Oligomer
Monomer
TAMRA
anti-Flag
anti-GSDME
b
C168
C235
C156
C45
C180
GSDME-CT
GSDME-NT
GSDME-FL
c
Denaturation
Reduction
Free Cys block
hpHA(-) Negative control
hpHA(+)
S-palmitoylation cleavage
MfTag (-)
MfTag labeling
MfTag (~5kDa)
hpHA(-)/MfTag(-)
hpHA(-)/MfTag(+)
hpHA(+)/MfTag(+)
d
WT
C45A
C156A
C168A
C180A
C235A
hpHA/MfTag
palm X2
palm X1
Long-exposure
f
PI positive (%)
Vector
FL (WT)
NT (WT)
C45A
C168A
C156A
C180A
C235A
C45A&C156A
C45A&C180A
C156A&C180A
C45A&C156A&C180A
e
Vector
NT (WT)
NT
C45A
C156A
C168A
C180A
C235A
C45A&C156A
C45A&C180A
C156A&C180A
C45A&C156A&C180A
FL (WT)
Propidium iodide (PI) /Hoechst 33342
Double staining